Atmos. Chem. Phys., 26, 16667–16682, 2026
https://doi.org/10.5194/acp-26-16667-2026
© Author(s) 2026. This work is distributed under
the Creative Commons Attribution 4.0 License.

Atmospheric Chemistry and Physics
Open Access
EGU

Research article

Tropical cyclone amplifies anthropogenic influences on aerosol-cloud interactions over the South China Sea

Hengjia Ou[1,2], Mingfu Cai[3], Haichao Wang[1], Xue Ni[4], Shixin Mai[1], Qibin Sun[5], Baoling Liang[6], Kunpeng Chen[7], Tao Deng[2], Sun Jiaren[3], Shengzhen Zhou[1], and Jun Zhao[1,✝]

[1]School of Atmospheric Sciences, Sun Yat-sen University, and Southern Marine Science and Engineering Guangdong Laboratory (Zhuhai), Zhuhai 519082, China
[2]Institute of Tropical and Marine Meteorology, China Meteorological Administration, Guangzhou 510640, China
[3]Guangdong Province Engineering Laboratory for Air Pollution Control, Guangdong Provincial Key Laboratory of Water and Air Pollution Control, South China Institute of Environmental Sciences, MEE, Guangzhou 510655, China
[4]Guangzhou Ecological and Agricultural Meteorological Center, Guangzhou 511430, China
[5]Guangzhou Sub-branch of Guangdong Ecological and Environmental Monitoring Center, Guangzhou 510006, China
[6]Dongguan Meteorological Bureau, Dongguan 523086, China
[7]State Key Laboratory of Regional Environment and Sustainability, School of Environment, Tsinghua University, Beijing 100084, China
✝deceased, October 2024

Correspondence: Mingfu Cai (mingfu0721@hotmail.com) and Haichao Wang (wanghch27@mail.sysu.edu.cn)

Received: 16 July 2026 – Discussion started: 24 August 2026
Revised: 26 October 2026 – Accepted: 9 November 2026 – Published: 23 November 2026

Abstract. Tropical cyclones can influence marine aerosol-cloud interactions by transporting continental anthropogenic pollutants over the ocean. However, this process and its impact remain poorly understood due to lack of direct measurements. Using shipborne measurements over the South China Sea (SCS) from 22 June to 5 July 2022, we investigated how TC Chaba altered aerosol physicochemical properties and cloud microphysical responses in its western region by modifying atmospheric circulation. As TC Chaba developed, its circulation altered regional transport pathways, shifting air masses from local marine origin to long-range transport from the Indochina Peninsula and causing pronounced increases in non-refractory submicron particulate matter (NR-PM_1) concentrations. Organic aerosol (OA) increased from 14.6 % to 44.9 % of NR-PM_1 after the influence of TC Chaba, mainly due to enhanced oxygenated OA (OOA) from long-range transport together with enhanced local heterogeneous oxidation, as indicated by the higher OA oxidation state and increasing OOA concentrations with O_x and relative humidity. These changes led to a $\sim$ 60 % decrease in aerosol hygroscopicity (κ), while an $\sim$ 27 % increase in κ_{OA}, which outweighed the modest particle size increase and resulted in a lower bulk activation ratio. Furthermore, CCN concentrations increased by up to sixfold because of enhanced aerosol concentrations. Combined observations and cloud parcel simulations indicate that the aerosol perturbations decreased cloud droplet effective radius by 11 %–37 % and increased the autoconversion radius by 6 %–26 %, enhancing cloud reflectivity and suppressing warm-rain formation. Satellite observations further confirmed smaller cloud droplets. These results demonstrate a strong TC influence on marine cloud microphysics and radiative effects.

Published by Copernicus Publications on behalf of the European Geosciences Union.

1 Introduction

Marine aerosols play an important role in the Earth's radiation budget and climate system (Chen et al., 2014; IPCC, 2021). However, substantial uncertainties remain in quantifying their radiative effects, largely due to their indirect influence on clouds (Wall et al., 2023; Qiu et al., 2024; Lu and Seinfeld, 2005). By acting as cloud condensation nuclei (CCN), marine aerosols affect cloud formation, lifetime, and albedo, yet these processes are still difficult to constrain in climate models (Wang et al., 2011; Boucher and Lohmann, 1995). In the remote marine boundary layer (MBL), natural aerosols, like sea salt aerosols, often dominate the CCN population (Kristensen et al., 2016; King et al., 2012). In contrast, marginal seas near continental outflow are frequently influenced by anthropogenic emissions and biomass burning plumes, creating mixed air masses with both marine and continental characteristics (Liu et al., 2013; Qin et al., 2024). This mixture increases aerosol loading and alters particle composition and hygroscopicity, thereby modifying CCN activity-which means the ability of aerosols to serve as CCN-and introducing considerable uncertainty into regional aerosol–cloud interaction (ACI) assessments (Jose et al., 2020). Model ensemble experiments reveal that uncertainties in marine aerosol parameterizations, cause global mean radiative forcing variations of about ± 0.3–$0.4\,\mathrm{W\,m^{-2}}$ (Bhatti et al., 2026). Observational constraints further suggest that reducing these parameterization uncertainties may decrease radiative forcing uncertainty by up to 20 % (Regayre et al., 2020). These findings underscore that variations in aerosol physicochemical properties are a key driver of ACI uncertainty, particularly over marine environments.

The South China Sea (SCS) is a typical marginal sea, surrounded by regions with substantial anthropogenic influence including southern China, the Indochina Peninsula, the Philippine Archipelago, and the Malay Peninsula – which makes it particularly sensitive to continental outflow and the long-range transport of air pollutants (Cai et al., 2020; Ou et al., 2025). The region is also frequently traversed by tropical cyclones (TCs) (Wang et al., 2007, 2014a). TCs influence atmospheric aerosols over the SCS through two main pathways: (1) TC-related precipitation effectively scavenges airborne particles (Lin and Huang, 2025; Chen et al., 2010); (2) the strong TC-induced circulation significantly modifies regional airflow, leading to shifts in the air masses reaching the SCS, and altering the physicochemical properties of aerosols consequently (Liang et al., 2021). Furthermore, TC-driven changes in aerosol properties can modulate cloud formation and precipitation processes, which in turn may affect TC intensity and lifetime (Wang et al., 2023, 2014b). However, quantifying the combined impacts of these TC-driven processes on aerosol physicochemical properties and subsequent cloud formation in the marine boundary layer (MBL) remains a major observational challenge.

Current understanding largely relies on satellite products, model simulations, and sparse land-based observations, which cannot resolve the rapid in situ changes within the MBL during and after TC passage. Previous satellite and modeling studies suggest that anthropogenic emissions may increase the occurrence of nearshore TCs and intensify TC-related precipitation, while suppressing TC strength and slowing development (Wang et al., 2014b, 2023). Coastal measurements have also shown that TCs can worsen ozone and $PM_{2.5}$ pollution in the Southern China (Shao et al., 2022; Wang et al., 2022). However, observational evidence over the ocean is still lacking, particularly regarding how TCs modify aerosol physicochemical properties and cloud microphysical processes. Closing this gap is essential for understanding the effects of TCs on ACI and their implications for regional climate.

In this study, a comprehensive shipborne observation campaign was conducted over the SCS, which captured the complete life cycle of TC Chaba. These unique measurements allow us to systematically examine how TC-driven alterations in atmospheric circulation reshape aerosol physicochemical properties, modulate CCN activities, and ultimately influence cloud microphysical processes in the marine boundary layer.

2 Method

2.1 Cruise information

A 15 d shipboard measurement was conducted from 20 June to 5 July 2022 in the SCS aboard the "Sun Yat-sen University" vessel, during the active summer monsoon period when the region was predominantly influenced by the southwest monsoon (Fig. S1). The vessel departed from Gaolan Port (Zhuhai), traveled to the vicinity of the Xisha Islands, and primarily operated – while also performing TC-avoidance maneuvers – in the waters south of Hainan Island and east of Vietnam, before returning to Gaolan Port (Fig. 1j). All instruments were put in a chamber in temperature-controlled chamber. The sample line was from the window of chamber to the driving room which is about 20 m from sea surface level. During the shipborne campaign, the observations covered the full life cycle of a TC event. TC Chaba began to influence the circulation over the SCS around 28 June, was officially named by the China Meteorological Administration on 29 June and was removed from the naming list on 4 July (Fig. 1c–i). Although Chaba was officially named on 29 June, a tropical disturbance had formed on 26 June and developed into a tropical depression by 28 June (Fig. S2), as classified by the Philippine Atmospheric, Geophysical and Astronomical Services Administration (PAGASA) and the Japan Meteorological Agency (JMA). Based on the above information, the period from 22 to 27 June is defined as the pre–TC period, and the period from 28 June to 4 July is defined as the post–TC Chaba period in this study.

2.2 Instruments

The chemical composition of non-refractory submicron particulate matter (NR-PM_1), including sulfate, nitrate, organics, ammonium, and chloride, was measured using a time-of-flight aerosol chemical speciation monitor with a standard vaporizer (SV-ToF-ACSM; Aerodyne Inc., USA). The instrument operated with a time resolution of ∼ 10 min. Ionization efficiency (IE) and relative ionization efficiency (RIE) were calibrated using ammonium nitrate (NH_4NO_3) and ammonium sulfate ($(NH_4)_2SO_4$) before and after each campaign. The nitrate IE values were 112.4 ions pg^{-1}. The RIE values for ammonium were 3.43, while those for sulfate were 0.77. The collection efficiency (CE) was 0.5. Assuming an average aerosol density of 1.5 g cm^{-3} (Geller et al., 2006), the mass concentrations from the SMPS and ToF-ACSM showed strong correlations, with coefficients of 0.84 (Fig. S3).

Size-resolved CCN activity was measured using the scanning mobility CCN analysis (SMCA) method proposed by Moore et al. (2010). The setup consisted of a scanning mobility particle sizer (SMPS) coupled with a cloud condensation nuclei counter (CCNc; CCNc-200, DMT Inc., USA) (Fig. S4). The SMPS included a differential mobility analyzer (DMA; model 3082, TSI Inc.) and a condensation particle counter (CPC; model 3756, TSI Inc.). The SMPS and CCNc were used to measure particle number size distributions (PNSD) and size-resolved CCN number concentrations across mobility diameters of 12–593 nm. The detail setting was described in the Sect. S1.

Before each campaign, the CCNc was calibrated at every SS using $(NH_4)_2SO_4$ particles. A detailed description of the calibration and instrument configuration is provided in Cai et al. (2018). Cai et al. (2018) The overall uncertainty of the size-resolved particle number concentration measured by the system is approximately 5 %–6 % (Moore et al., 2010).

The trace gases (NO, NO_2, O_3, and SO_2) were measured by gas analyzers (TELEDYNE API Inc.), which were calibrated with standard gases before the measurement. The timeseries of trace gases was shown in Fig. S5.

To ensure the reliability of atmospheric measurements over the SCS and to minimize contamination from ship emissions, data quality controls were conducted, which was detailed in Sect. S2. 90.1 % of the data (10 min resolution) were classified as clean and retained for subsequent analysis. During the measurement period, technical issues with the ToF-ACSM resulted in a prolonged data gap before 27 June, while a data acquisition software failure caused a data loss in the SMPS measurements from 28 to 29 June.

2.3 Data analysis

2.3.1 Organic aerosol positive matrix factorization

In this study, PMF was applied to the organic aerosol (OA) mass spectra measured by the SV-ToF-ACSM which was described detailly in Sect. S3; thus, the analysis is referred to as OA PMF. Diagnostic plots used to evaluate the PMF solution are shown in Fig. S6. Three OA factors were resolved, including two primary OA factors – hydrocarbon-like OA (HOA) and seasalt-related OA – and one secondary OA factor, oxygenated OA (OOA) (Fig. S7). OOA constituted the largest fraction of OA, accounting for 82.6 % (Fig. S8a). Its oxidation indicator, the fraction of m/z 44 (CO_2^+, f_{44}), was 0.31 – similar to the f_{44} value of LVOOA (0.31) observed over the SCS in 2018 (Liang et al., 2021), and slightly lower than that of OOA (0.33) measured in 2019 (Fig. S8b) (Sun et al., 2023). HOA was the second largest contributor (15.6 %). Its mass spectrum is characterized by prominent C_nH_{2n-1} and C_nH_{2n+1} ion series (e.g., m/z 41, 43, 55, 57, 69, and 71) (Fig. S7a1), consistent with the mean HOA profile reported by Ng et al. (2011a). The mass spectrum of sea-salt-related OA showed peaks at m/z 58 and 60, which may be associated with chloride-containing ions. Van den Born et al. (2026) experimentally demonstrated that CV-ToF-ACSM can detect a fraction of NaCl. Although NaCl is generally difficult to vaporize in SV-ToF-ACSM, a small fraction may still be detected (1.7 %). Given its small and relatively stable contribution, this factor was interpreted as a mixture of sea salt and OA and was therefore named Sea-salt-related OA in this study.

2.3.2 Size-resolved cloud condensation nuclei activity

The size-resolved number concentrations of total particles and CCN were obtained from the SMPS and CCNc using the SMCA method. The activation diameter was derived by fitting the activation ratio ($AR = N_{CCN}/N_{CN}$) as a function of dry particle diameter at each SS using the following sigmoid function:

$$AR = \frac{B}{1 + \left(\frac{D_P}{D_{50}}\right)^C} \quad (1)$$

where AR is the size-resolved AR, D_P indicates dry particle diameter (nm); B, C, and D_{50} are the three fitting parameters, representing the asymptote, the slope, and the inflection point of the sigmoid, respectively (Moore et al., 2010). The parameter D_{50}, also referred to as the critical diameter, corresponds to the particle size at which 50 % of particles activate at a given SS. The SMCA fitting results obtained in this study are shown in Fig. S9.

The hygroscopicity parameter κ, which characterizes CCN activity within the κ-Köhler theory, was calculated following (Petters and Kreidenweis, 2007):

$$\kappa = \frac{4A^3}{27{D_{50}}^3(\ln S_c)^2}, A = \frac{4\sigma_{s/a}M_w}{RT\rho_w} \quad (2)$$

where ρ_w is the density of pure water which value is about 997.04 kg m^{-3} at 298.15 K, M_W is the molecular weight of water which value is 0.018 kg mol^{-1}, $\sigma_{s/a}$ represents the

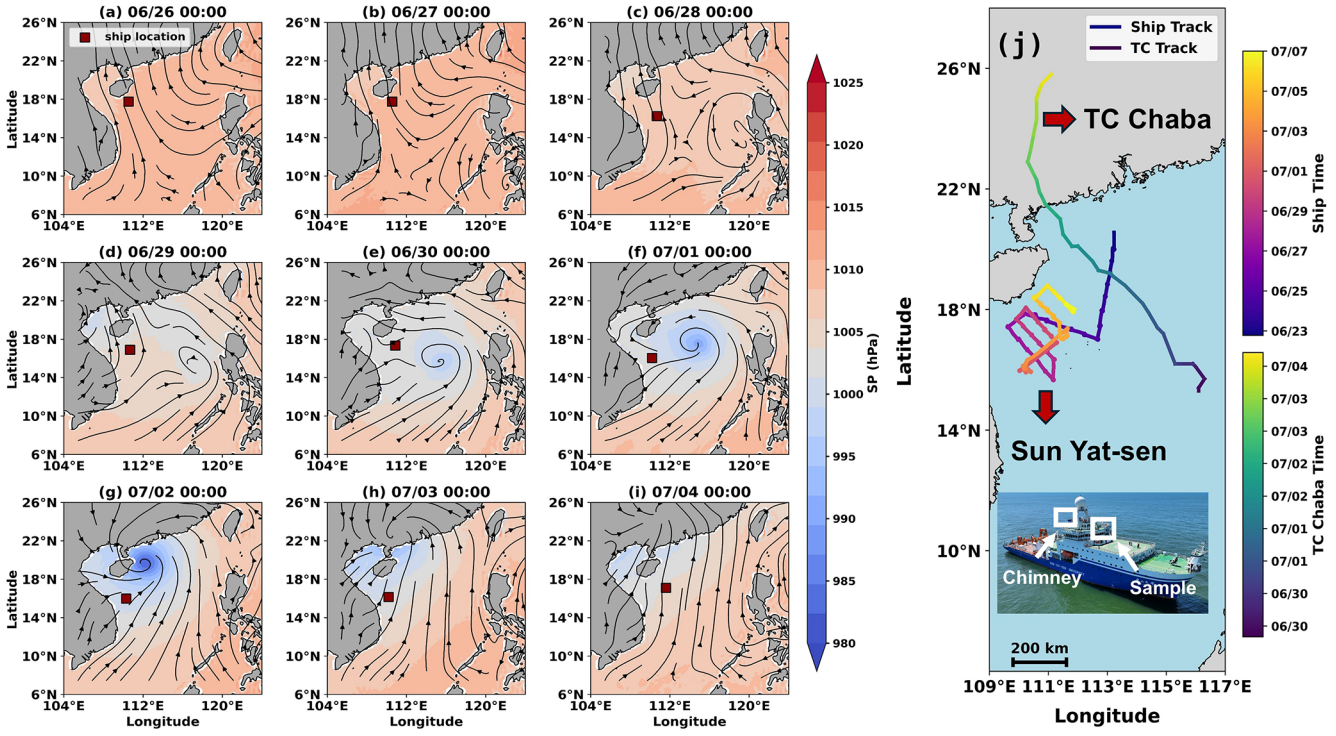


Figure 1. Changes in surface pressure (SP) and wind fields over the South China Sea before and after the formation of Tropical Cyclone (TC) Chaba (26 June–4 July, **a**–**i**). The cruise track of "Sun Yat-sen" research vessel, the sampling locations, the ship exhaust stack position, and the track of TC Chaba.

surface tension of the solution-air interface and is assumed to be equal to the surface tension of pure water ($\sigma_{s/a} = 0.0728\,\mathrm{N\,m^{-1}}$ at 298.15 K), R is the universal gas constant ($8.314\,\mathrm{J\,mol^{-1}\,K^{-1}}$), and T denotes thermodynamic temperature in kelvin, which is 298.15 K in this study. Additionally, it should be noted that the estimated κ values refer to particles with the D_{50}.

Due to the malfunction of column B, the N_{CCN} was derived from size-resolved AR at a given SS obtained using the SMCA method, together with the measured N_{CN}. N_{CCN} was calculated following, Cai et al. (2018) using the equation:

$$N_{CCN}(SS) = \int_0^{\infty} AR(SS,\ D_P) N_{CN}(D_P)\,dD_p \quad (3)$$

where N_{CCN} (SS) is the CCN number concentration at a specific SS, AR(SS, D_p) is the ratio of N_{CCN} at a specific SS to N_{CN} on a specific diameter from the SMCA method and N_{CN} (D_P) is the particle number concentration at a specific diameter (D_P). Because direct measurements of total N_{CCN} were unavailable, the values derived from Eq. (3) are treated as the observed CCN number concentrations ($N_{CCN,obs}$) in this study. Previous studies have demonstrated that this approach – estimating size-resolved CCN using a single column of the CCNc-200 – yields result that closely match those obtained from direct measurements using the other column of the instrument (Lathem and Nenes, 2011; Meng et al., 2014). These findings support the robustness and reliability of the method.

After obtaining the value of $N_{CCN,obs}$, the bulk AR can be calculated as follows:

$$\mathrm{bulkAR}(SS) = \frac{N_{CCN,obs}(SS)}{N_{CN,tot}} \quad (4)$$

where the $N_{CN,tot}$ represents the total particle number concentration.

2.3.3 Cloud parcel model simulation

To integrate our observations and further investigate how variations in aerosol physicochemical properties influence cloud microphysics, we used the 0-D cloud parcel model Pyrcel to simulate aerosol activation into cloud droplets at cloud base. Based on these simulations, we quantified the impact of changes in cloud droplet number concentration (N_C) on cloud microphysical properties during pre-TC Chaba and post-TC Chaba periods. The Pyrcel model describes the growth and evolution of cloud droplet size distributions from a prescribed aerosol population. The model was initialized with aerosol particle size distributions for the Aitken and accumulation modes observed during pre-TC Chaba and post-TC Chaba periods (Fig. S9). During pre-TC Chaba and post-TC Chaba periods, the geometric mean diameters of the Aitken and accumulation modes were 57 and 156 nm and 60

and 123 nm, respectively. The D_{50} values at of 0.4 % SS and 0.2 % SS were 54 and 87 nm during pre-TC Chaba period and 74 and 127 nm during post-TC Chaba period, respectively. Following Pöhlker et al. (2016), we selected the SS level with a D_{50} closest to the geometric mean diameter of each mode to represent its hygroscopicity. Although the D_{50} at 0.2 % SS was smaller than the accumulation-mode geometric mean diameter during pre-TC Chaba period, the size-dependent hygroscopicity varied relatively little as particle size increased after 54 nm. Thus, the hygroscopicity measured at 0.2 % SS was considered representative of the accumulation mode. Meteorological inputs, including average temperature, pressure, and relative humidity, were also prescribed for the pre- and post-Chaba periods.

In the Pyrcel simulations, updraft velocity (w) is a key input parameter that determines the maximum supersaturation. During most of the observation period, the distance between the center of TC Chaba and the research vessel ranged from 400 to 800 km. After the evening of 3 July, this distance exceeded 800 km as the cyclone moved farther away from the vessel. Previous studies have reported updraft velocities of approximately 0.1–2 m s^{-1} in the outer regions of tropical cyclones and typical cyclone sizes of 700–800 km (Black et al., 1996; Pérez-Alarcón et al., 2021). Considering the distance between the vessel and the cyclone center, together with the reported updraft velocities in the outer regions, we prescribed updraft velocities ranging from 0.1–2 m s^{-1} in the simulations. Because w cannot be directly measured, a range of 0.1–2 m s^{-1} was prescribed, representing typical updraft conditions at distances of approximately 400–500 km from the TC center (Black et al., 1996). It is noted that the minimum distances between our ship location and center of TC Chaba were 400–500 km. Under the actual meteorological conditions and assuming adiabatic ascent, the corresponding SS at cloud base ranged from 0.03 % to 0.23 % across this w. The detailed input parameters and simulation results were presented in Tables S1 and S2, respectively.

2.3.4 Cloud microphysical parameter calculation

Based on the Pyrcel simulation, the following equations were used to quantify two key ACI effects – the Twomey effect and the Albrecht effect – using the cloud droplet effective radius (r_e) and the critical radius of autoconversion process (r_c). A larger r_e indicates a decrease in cloud albedo, whereas a larger r_c indicates a reduced likelihood of cloud droplets converting into raindrops (Wang et al., 2019).

r_e can be calculated as follows:

$$r_e = \beta\left(\frac{3q}{4\pi\rho_w N_c}\right)^{1/3} \quad (5)$$

Here, β is a scaling factor, ρ_w is water density, and N_C is cloud droplet concentration from Pyrcel simulation. Previous studies have analyzed the factors affecting β and proposed corresponding parameterizations (Liu et al., 2008; Rotstayn and Liu, 2009). The liquid water content (LWC), q, is given by:

$$q = \int_0^\infty \frac{4}{3}\pi r^3 \rho_w n(r)\mathrm{d}r \quad (6)$$

where $n(r)$ is the cloud droplet number size distribution. Because droplet size distributions were not directly measured in this study, a gamma distribution was assumed, expressed as $n(r) = N_0 r^\mu \exp(-\lambda r)$, where r is the droplet radius, N_0 is the intercept parameter, μ is the shape parameter, and λ is the slope parameter. Typical Gamma-distribution parameters for marine environment are $N_0 = 8 \times 10^{-30}$, $\mu = 4$, and $\lambda = 2 \times 10^{-5}$ (Miles et al., 2000; Seifert and Beheng, 2006).

To isolate the influence of N_C on r_e, β was assumed to be constant. This assumption is commonly adopted in climate models to reduce uncertainties in other parameters and simplify the analysis (Quaas et al., 2004).

The r_c is parameterized as (Liu et al., 2006):

$$r_c \approx 4.09 \times 10^{-4} \beta^{1/6} \frac{N_c^{1/6}}{q^{1/3}} \quad (7)$$

where $\beta = 1.15 \times 10^{23}$ is an empirical constant. Based on the estimated critical radius, this study further evaluates the impact of anthropogenic influences on the Albrecht effect.

2.3.5 Satellite data and backward trajectory analysis

To further investigate aerosol-cloud interaction, we acquired the liquid cloud effective radius data from the MCD06COSP_D3_MODIS product for comparison (Webb et al., 2017). Specifically, we extracted the Cloud_Particle_Size_Liquid variable, which represents the liquid cloud droplet effective radius retrieved primarily from near-infrared observations at a wavelength of 2.1 µm (Platnick et al., 2017). Following the MODIS Collection 6.1 quality-control criteria implemented in the COSP framework, we retained valid retrievals according to the applied cloud-pixel selection criteria. The data were aggregated onto a 1° × 1° grid, and we used the resulting valid-pixel coverage without applying additional pixel-count thresholds. Since the SCS is located in the subtropics and tropics and our observations were conducted within the boundary layer, we specifically focused on the particle size of low-altitude liquid warm clouds, excluding ice clouds. We defined a study area between 12 and 18° latitude and 109 and 112° longitude (which encompassed the ship's position). Within this region, we calculated the average Cloud particle size liquid values for pre-TC Chaba period and post-TC Chaba period. The MCD06COSP_D3_MODIS product provides daily averaged values, and examples representing these two periods and calculation range are presented in Fig. S11.

Backward trajectory calculations were conducted using MeteoInfo, an open-source atmospheric analysis package (Wang, 2014), to identify potential source regions. Weekly

GDAS1 (Global Data Assimilation System, 1° resolution) meteorological fields were obtained from the NOAA Air Resources Laboratory (ARL) (https://www.ready.noaa.gov/gdas1.php, last access: 12 December 2025). Backward trajectories were computed every hour for the ship location, producing 72 h trajectories at an arrival height of 500 m.

3 Result

3.1 Overview

The timeseries of aerosol size distribution, meteorological parameters (RH, T, precipitation, and pressure), CCN number concentration (N_{CCN}) at different SS, and κ were shown in Fig. 2.

Compared to the pre–TC Chaba period, aerosol concentrations increased substantially during the post–TC period, accompanied by pronounced shifts in their physicochemical properties, which are described in detail in the following section. Meteorological conditions also changed notably during this period. Air temperature (T) decreased slightly, with the daytime maximum dropping from $\sim 35\,^{\circ}C$ during the pre-TC period to $\sim 24\,^{\circ}C$ during the post-TC period (Fig. 2b). Relative humidity (RH) increased gradually, reaching nearly 100 % on 1 July during the post-TC period, coinciding with the only rainfall event observed (Fig. 2b). Atmospheric pressure (P) also declined from ~ 1005 hPa to below 1000 hPa during the transition from the pre–TC to post-TC period and then gradually recovered to around 1000 hPa as the system weakened (Fig. 2c). It should be noted that no significant precipitation occurred during the observation period under the influence of TC Chaba, except on 1 July. The precipitation during this period resulted in substantial wet scavenging of aerosols, leading to pronounced decreases in both aerosol number concentration and mass concentration.

The average aerosol particle number concentration (N_{CN}) was 4345 cm^{-3}, slightly higher than the values measured over the SCS in 2014 ($\sim 1356\,cm^{-3}$) and 2018 ($\sim 3400\,cm^{-3}$) but lower than those reported in 2021 (6966 cm^{-3}) (Atwood et al., 2017; Cai et al., 2020; Ou et al., 2025). In contrast to the 2014 and 2021 measurements – both dominated by Aitken-mode particles – the present campaign was characterized by a predominance of accumulation-mode particles, which accounted for 50.6 % of the total N_{CN}, followed by the Aitken (46.8 %) and nucleation modes (4.1 %). Besides, the average N_{CCN} ranged from 902 to 2552 cm^{-3} at 0.2 %–0.7 % SS. These values were generally consistent with the variability in N_{CN}: they were higher than those measured over the SCS in 2014, similar to the levels observed in 2018, and lower than the concentrations reported in 2021 (Atwood et al., 2017; Cai et al., 2020; Ou et al., 2025).

The average NR-PM_1 concentration was $7.30 \pm 4.24\,\mu g\,m^{-3}$, lower than the values measured in the South China Sea during the summers of 2018 (9.11 $\mu g\,m^{-3}$) and 2019 (10.65 $\mu g\,m^{-3}$), but higher than that observed in 2021 (3.76 $\mu g\,m^{-3}$) (Sun et al., 2023; Liang et al., 2021). Sulfate was the dominant component (42.8 %), followed by organics (42.3 %), ammonium (9.1 %), nitrate (3.2 %), and chloride (2.6 %). The mean organic fraction exceeded those reported for the SCS in 2018, 2019, and 2021, and was more comparable to values observed in the Mediterranean region (Mallet et al., 2019). Given that organic aerosols in the SCS are strongly influenced by anthropogenic emissions, the elevated organic contribution in this study suggests a greater impact of human activities relative to previous campaigns.

The average aerosol hygroscopicity parameter (κ) ranged from 0.34 to 0.43 at 0.2 %–0.7 % SS, lower than the values observed over the SCS in the summer of 2021 (0.47–0.54 from 0.2 % to 0.4 % SS) but comparable to those reported in 2018 (0.38 at 0.18 % SS) (Ou et al., 2025; Cai et al., 2020). The average bulk activation ratio (AR) varied from 0.28 to 0.72 across the same supersaturation range, remaining below the levels measured in both 2021 (0.37–0.87 at 0.2 %–0.7 % SS) and 2012 (0.47–0.85 at 0.15 %–0.71 % SS) (Ou et al., 2025; Atwood et al., 2017).

During the observation period, TC Chaba formed over the South China Sea and exerted a significant influence on the region. As the vessel location remained on the western region of the TC, the effects on aerosol physicochemical and cloud microphysical properties discussed below represent those observed on the western region of TC Chaba.

3.2 Tropical cyclone Chaba-induced changes in aerosol physicochemical properties

Air masses over SCS changed markedly following the development of TC Chaba (Fig. S12). During pre-TC Chaba period, the region was dominated by local marine air masses, with a small fraction transported over Luzon Island. After the establishment of Chaba's circulation, air masses were primarily transported from the Indochina Peninsula. Correspondingly, the NR-PM_1 concentration increased from 4.51 to 8.84 $\mu g\,m^{-3}$. During the pre-TC Chaba period, NR-PM_1 was dominated by sulfate (67.3 %), exhibiting a typical marine air-mass signature consistent with the backward-trajectory analysis. After the influence of TC Chaba, aerosol composition shifted substantially, with the organic aerosol (OA) fraction increasing from 14.6 % to 44.9 % and becoming the dominant aerosol component (Fig. 3a and b). This increase was mainly driven by OOA, whose contribution rose from 9.8 % to 38.5 %. HOA and BBOA also increased but contributed much less than OOA, suggesting oxidation of these components during long-range transport.

Changes in the PNSD further illustrate the substantial impact of TC Chaba on aerosol physicochemical properties. The PNSD data were analyzed by fitting three characteristic modes: Nucleation, Aitken, and Accumulation. Subsequently, the effective diameter (D_{eff}) was also calculated from PNSD data. The detailed methodology for this procedure is described in Sect. S4. During post-TC Chaba period,

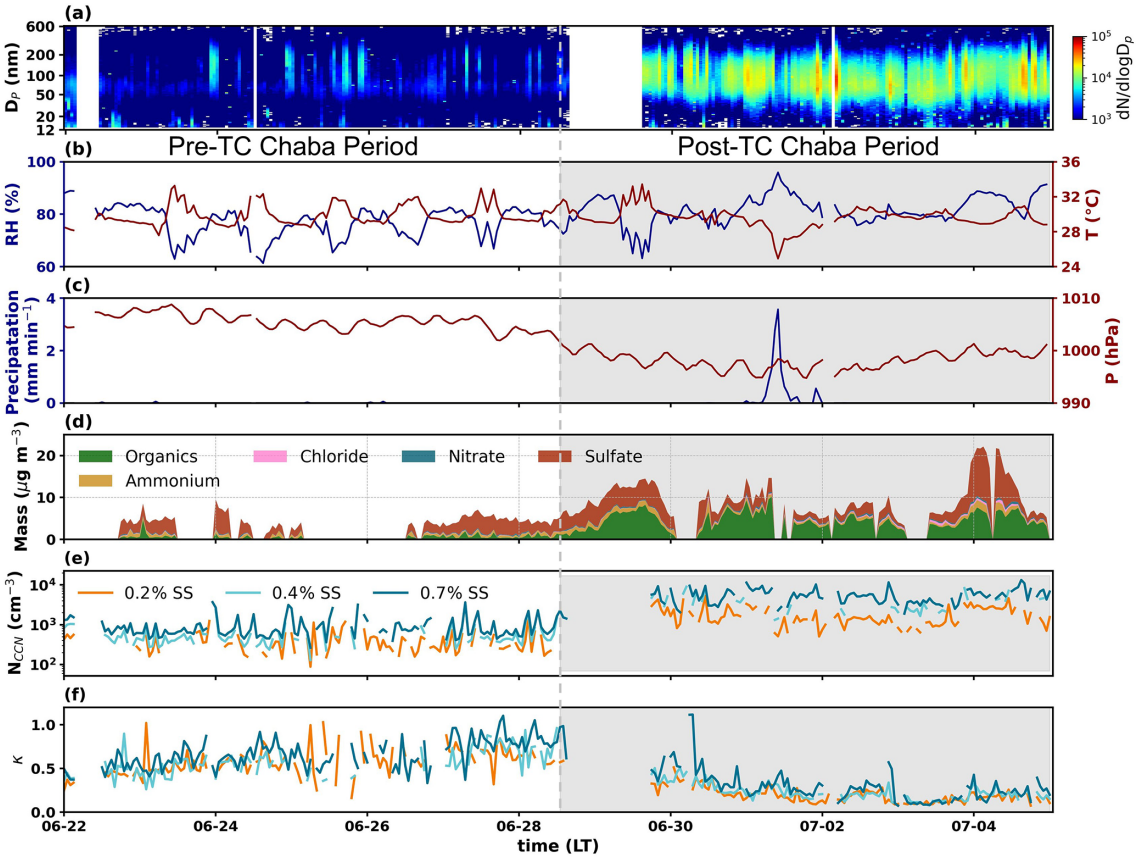


Figure 2. Timeseries of particle number size distribution **(a)**, relative humidity (RH) and air temperature (T) **(b)**, precipitation and pressure (P) **(c)**, mass concentration of different aerosol composition **(d)**, cloud condensation nuclei number concentration at different supersaturations (SS) **(e)**, and aerosol hygroscopicity parameter (κ) at different SS.

the total aerosol number concentration increased markedly, driven primarily by enhancements in the aitken and accumulation modes (Fig. 3c and d). The accumulation-mode contribution increased from 37.4 % to 49.1 %, indicating substantial aerosol aging and particle growth associated with long-range transport and secondary organic aerosol formation.

Besides, to investigate the drivers of OOA enhancement, we examined its relationship with meteorological and chemical parameters. During the post-TC Chaba period, OOA increased rapidly when relative humidity exceeded 75 %, accompanied by an increase in oxidation state (Fig. 4a and b). In addition, both OOA and total OA exhibited stronger positive correlations with O_x ($O_3 + NO_2$) during the post-TC period than during the pre-TC period, suggesting that Chaba-induced transport from the Indochina Peninsula strengthened the atmospheric oxidation capacity over the SCS and consequently promoted OA oxidation (Fig. 4d and e). These changes coincided with a shift in air-mass origin toward the Indochina Peninsula, suggesting that both air-mass transport and changes in the atmospheric oxidation environment were associated with the observed OOA enhancement. However, these concurrent changes do not allow the contributions of transported aged OOA and local secondary formation to be distinguished. To further examine the potential contribution of secondary formation, we normalized OOA by ΔCO to partly account for changes in boundary-layer mixing and dilution. The OOA/ΔCO ratio showed a clear nighttime enhancement (Fig. S16), suggesting that the OOA increase cannot be explained solely by boundary-layer evolution. This pattern is consistent with a contribution from secondary OA formation, although the effects of air-mass transport and other meteorological processes cannot be excluded. Overall, our results suggest that both long-range transport and secondary formation likely contributed to the observed OOA enhancement.

Driven by the increased contribution of OA, particularly the enhanced fraction of OOA, κ decreased substantially during post-TC Chaba period. Specifically, κ ranged from 0.58–0.66 at 0.2 %–0.7 % SS before Chaba influence but declined sharply to 0.20–0.31 over the same SS range afterward (Fig. 3c and d). During pre-TC Chaba period, the overall κ was comparable to values reported by Atwood et al. (2017) over the SCS, indicating a dominant marine air-mass influence. In contrast, during post-TC Chaba period, κ approached those

measured in urban Guangzhou (Cai et al., 2018), further proving that Chaba-induced circulation changes facilitated the transport of anthropogenic aerosols from the Indochina Peninsula into the SCS.

To further quantify the impact of OA on κ, we applied a linear parameterization between κ and the organic mass fraction (f_{OA}), as described by previous research (Huang et al., 2022b; Bhattu et al., 2016). κ at 0.2 % SS were used for this analysis because this lower SS better represents the hygroscopicity of larger particles and aligns more closely with the aerosol size range measured by the SV-ToF-ACSM (Ng et al., 2011b). The resulting $\kappa - f_{OA}$ relationships reveal a clear reduction in slope after the influence of Chaba under the dominance of Indochina air masses compared to marine conditions, which is consistent with the findings in the remote marine enviroments (Huang et al., 2022b). Notably, the slope obtained under marine influence in this study is lower than that reported for remote marine, likely reflecting the relatively less pristine background conditions of the SCS even before the influence of TC Chaba. This interpretation is supported by long-term AERONET observations showing continental aerosol influence over the SCS and aircraft measurements reporting substantial anthropogenic aerosol contributions from industrial emissions, ship emissions, and biomass burning in the region (Chen et al., 2023; Miller et al., 2023).

Based on the $\kappa - f_{OA}$ fits, κ_{OA} was defined as the κ value at $f_{OA} = 1$. The estimated κ_{OA} increase from 0.11 during pre-TC Chaba preiod to 0.15 during post-TC Chaba period, representing an approximately 27 % increase (Fig. 4c and f). The κ_{OA} is related to its oxidation state, with higher oxidation leading to greater hygroscopicity. During post-TC Chaba period, the fraction of OOA in total OA increased compared to the pre-TC Chaba period, thereby enhancing the overall oxidation level of OA, as further supported by the increase in the $m/z44$-to-$m/z43$ ratio from 4.78 to 6.36. Despite the increase in κ_{OA}, the bulk κ decreased significantly during post-TC Chaba period. This apparent discrepancy can be explained by the relatively low hygroscopicity of OA compared to inorganic components and its obviously higher fraction in total aerosol mass during post-TC Chaba period. In addition, OA measured by the SV-ToF-ACSM was mainly associated with particles around 600 nm, whereas κ at 0.2 % SS represents the hygroscopicity of particles around 100 nm. Studies conducted on the east coast of the Baltic Sea and Fukue Island showed that the average f_{OA} increases by approximately 15 % from 100 to 600 nm (Takami et al., 2005; Ovadnevaite et al., 2007). This change in f_{OA} would alter the fitted slopes by 10.5 % and 12.5 % during the pre-TC and post-TC Chaba periods, respectively, introducing uncertainty into the estimated result.

3.3 CCN activity response to aerosol property changes

Changes in the physicochemical properties of aerosols can influence their ability to activate into CCN which was also named CCN activity. It is primarily governed by two factors: particle size distribution and chemical composition. Chemical composition affects activation mainly by altering aerosol hygroscopicity (Petters and Kreidenweis, 2007). Here, we evaluate variations in CCN activity by examining changes in these two controlling factors. The bulk AR is used as the key metric to quantify CCN activity.

As described above, although the aerosol size distribution shifted toward larger particles because of the enhanced contribution from the accumulation mode, D_{eff} increased only slightly, from 92 to 96 nm (∼ 4 %). In contrast, the decrease in aerosol hygroscopicity – driven by the substantial increase in organic aerosol fractions – was far more pronounced, which was described in previous section.

Considering the combined influence of these two factors, the bulk AR decreased from 0.33–0.80 at 0.2 %–0.7 % SS during pre-TC Chaba period to 0.24–0.73 during post-TC period (Fig. 5a). This indicates that the reduction in aerosol hygroscopicity exerted a stronger influence on CCN activation than the modest increase in particle size, making hygroscopicity the dominant driver of the observed decline in bulk AR. The decrease in bulk AR was also more pronounced at lower SS, consistent with the larger reduction in hygroscopicity for particles activated under low SS.

Although many previous studies have suggested that particle size distribution generally exerts a greater influence on CCN activity than aerosol hygroscopicity (Kuwata and Kondo, 2008; Dusek et al., 2006; McFiggans et al., 2006), our results demonstrate that hygroscopicity can become the controlling factor when changes in size distribution are relatively minor but decreases in hygroscopicity are substantial. The study in Western Pacific has shown that in clean oceanic environments, variations in aerosol hygroscopicity driven by marine biogenic emissions primarily regulate CCN activity (Kawana et al., 2022). Our findings further highlight that, under strong anthropogenic influence over marine regions, changes in OA fraction can influence aerosol hygroscopicity, thereby playing a crucial role in determining CCN activity.

3.4 Impacts on cloud microphysics and radiation effects

The influence of TC Chaba on aerosol physicochemical properties above points to a coherent chain of perturbations: the influx of anthropogenic aerosols from the Indochina Peninsula not only elevated particle concentrations but also substantially reduced aerosol hygroscopicity, which in turn suppressed CCN activity despite a modest increase in particle size. These shifts in aerosol properties could propagate further, with potential consequences for cloud microphysics over the SCS, which is discussed in this section. Cloud microphysics is influenced by two key mechanisms – the Twomey effect and the Albrecht effect. The Twomey effect describes how increases in N_{CCN} lead to higher cloud droplet number concentrations and smaller droplet sizes, thereby enhancing cloud reflectivity and exerting a cooling radia-

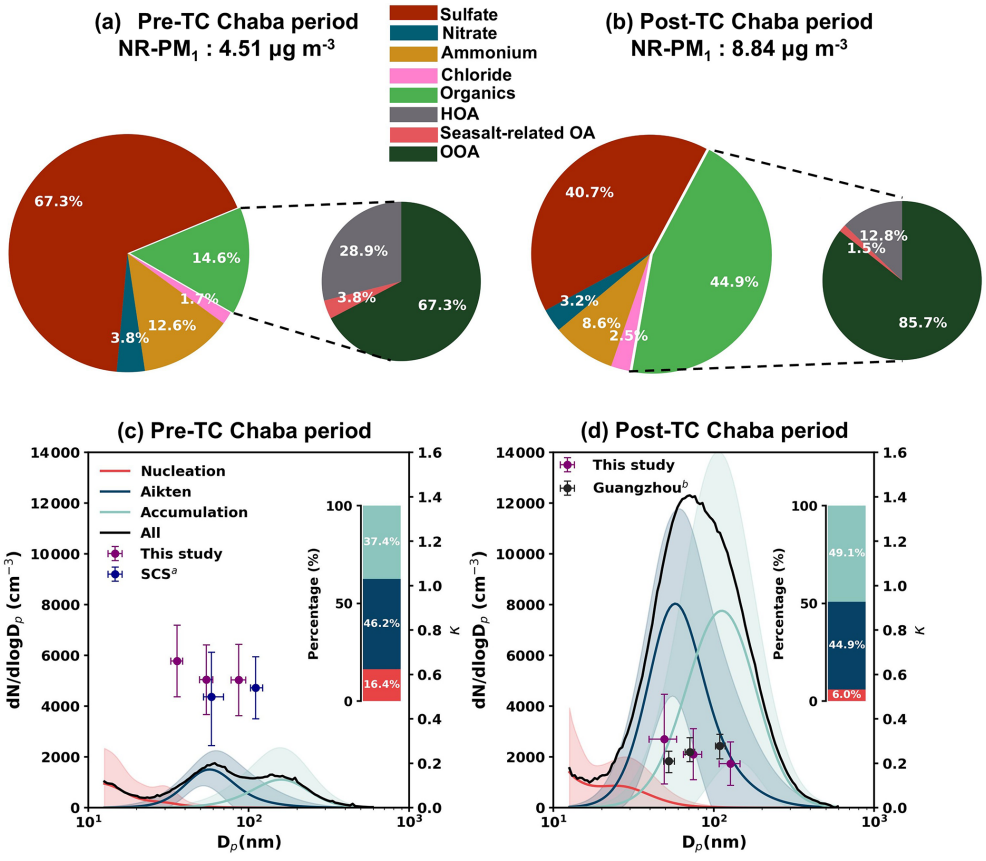


Figure 3. Aerosol composition mass concentration and fraction during pre-TC Chaba period **(a)** and post-TC Chaba period **(b)**; Particle number size distribution, different particle mode fraction, activation diameter (D_{50}), and aerosol hygroscopicity parameter (κ) during pre-TC Chaba period **(c)** and post-TC Chaba period **(d)**; In panels **(c)** and **(d)**, the blue error bars represent the D_{50} and κ values derived in this study. The blue error bars (SCS[a]) indicate measurements reported by Atwood et al. (2017) over the SCS, and the black error bars (Guangzhou[b]) denote observations from Cai et al. (2018) conducted in the urban area of Guangzhou, China. The barplot presents the fraction of three particle modes.

tive forcing (Twomey, 1959). In contrast, the Albrecht effect refers to the suppression of precipitation efficiency due to smaller droplet sizes, which reduces precipitation efficiency and extends cloud lifetime.(Albrecht, 1989) The cloud effective radius (r_e) and the critical diameter (r_c) represent the Twomey effect and Albrecht effect, respectively.

By analyzing the observed changes during pre-TC Chaba and post-TC Chaba periods, we assessed how shifts in aerosol properties modulated these two effects, providing insight into the microphysical and radiative implications of TC-driven aerosol perturbations over the SCS. Although the bulk AR decreased during post-TC Chaba period compared to pre-TC Chaba period, the marked increase in total N_{CN} resulted in a substantial enhancement of N_{CCN}. Across SS of 0.2 %–0.7 %, N_{CCN} rose from 400–951 cm^{-3} during pre-TC Chaba period to 1918–5981 cm^{-3} during post-TC Chaba period (Fig. 5b). In terms of change of N_{CCN}, the increase became more pronounced with rising SS during post-TC Chaba period, indicating that a larger number of smaller particles were activated as CCN.

The Pyrcel simulations linking the observed aerosol physicochemical properties to N_C are consistent with the observed N_{CCN}. Although the bulk AR decreased during post-TC Chaba period, the total activated particle number concentration increased due to the elevated N_{CN}. The simulation inputs are summarized in Table S2. Under the observed meteorological conditions and aerosol physicochemical properties, and within the prescribed updraft range, the critical maximum SS (S_{max}) was estimated to be ~ 0.03 %–0.23 %. These relatively low SS suggest that aerosol activation occurred within an aerosol–updraft sensitive regime according to Reutter et al. (2009), rather than a purely aerosol-limited regime (Reutter et al., 2009). This interpretation is supported by the pronounced dependence of N_C on both updraft velocity and aerosol concentration, as well as the reduction in S_{max} under enhanced aerosol conditions during the post-TC Chaba period (Table S2). The κ values assigned to the

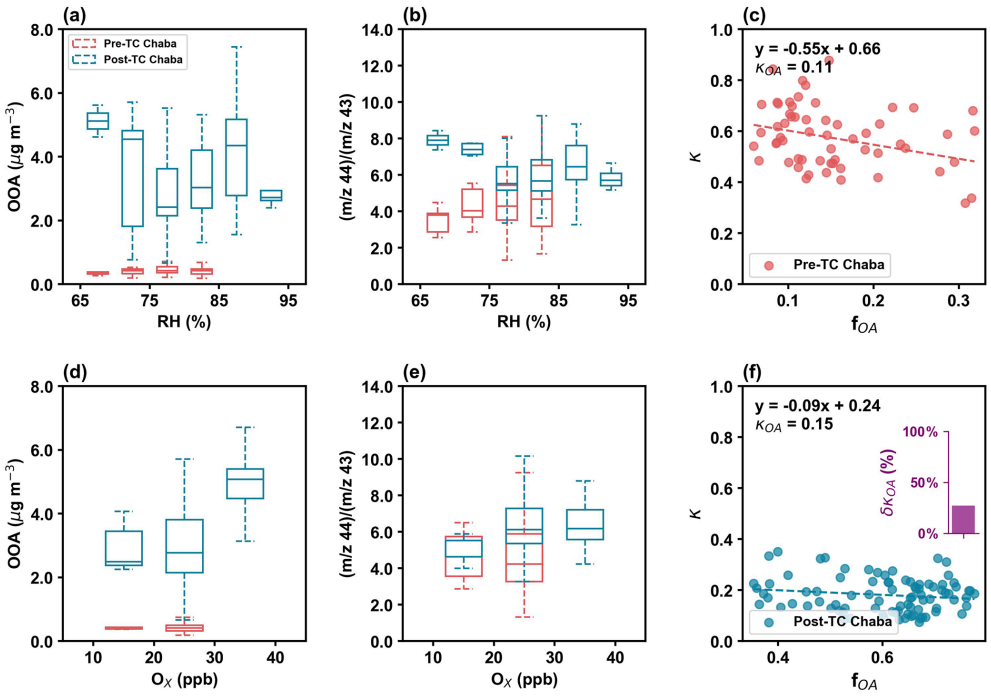


Figure 4. Comparison of Oxygenated Organic Aerosol (OOA) mass concentration and $m/z44/m/z43$ ratio as a function of Relative Humidity (RH) and O_x (O_3+NO_2) during pre-TC Chaba and post-TC Chaba periods **(a)** OOA (μg m^{-3}) vs. RH (%); **(b)** $m/z44/m/z43$ ratio vs. RH (%); **(d)** OOA (μg m^{-3}) vs. O_x (ppb); **(e)** $m/z44/m/z43$ ratio vs. O_x (ppb); **(c)** The linear parameterization between κ and the organic mass fraction (f_{OA}) during pre-TC Chaba period; **(f)** The linear parameterization between κ and the f_{OA} during post-TC Chaba period and the purple bar represents the decrease in κ_{OA}; The box plots illustrate the distribution of the data (whiskers: 10th and 90th percentiles; box: 25th, 50th (median), and 75th percentiles). Red boxes and circles represent data during pre-TC Chaba period, and blue boxes and circles represent data during post-TC Chaba period.

Aitken and accumulation modes may differ from their actual values. To assess the resulting uncertainty, we varied κ by ±50 %, based on reported size-dependent variations in κ at other observation sites (Pöhlker et al., 2016). During the pre-TC Chaba period, these variations changed the simulated concentrations by −8.78 % to +3.11 % across the tested updraft velocities. During the post-TC Chaba period, the changes were generally smaller, ranging from −10.74 % to +3.01 %, except at an updraft velocity of 0.3 m s^{-1}. At this velocity, a 50 % reduction in κ resulted in a 38 % difference in the simulated concentration. This larger difference was mainly due to the increase in S_{max} caused by the lower κ, which, combined with the model's limited resolution, led to a larger deviation in the simulated concentration. Overall, uncertainties in κ had only a small effect on the simulated N_C concentrations.

Based on the simulations, the r_e and r_c were derived for conditions during pre-TC Chaba and post-TC Chaba periods. As the updraft velocity increased from 0.1 to 2 m s^{-1}, r_e decreased by 11 %–37 %, with a diminishing rate of decrease at higher updraft velocities. This pattern suggests that the influence of TC Chaba increased N_C while reducing droplet size, consistent with an enhancement in cloud albedo.

In contrast, r_c exhibited the opposite response. Across the same updraft range, r_c increased by 6 %–26 %, indicating reduced efficiency in the conversion of cloud droplets to raindrops during post-TC Chaba period, thereby probably suppressing precipitation formation.

4 Discussions

Based on a shipborne observation during a TC event, our results show that TC-induced circulation changes can rapidly transform the marine boundary layer from a typical sulfate-dominated, highly hygroscopic marine background to a regime characterized by organic aerosol dominance, lower hygroscopicity, and substantially elevated aerosol concentrations associated with anthropogenic influence. During this transition, our results indicate that changes in hygroscopicity exert a stronger influence on CCN activity than changes in particle size distribution. This finding contrasts with results from other regions, where particle size distribution is often identified as the primary controlling factor for CCN activity and is as dominant control factor on aerosol activation in atmospheric models (Dusek et al., 2006). It suggests that models applied to marine regions periodically perturbed by continental outflow may systematically misrepresent N_{CCN} if hy-

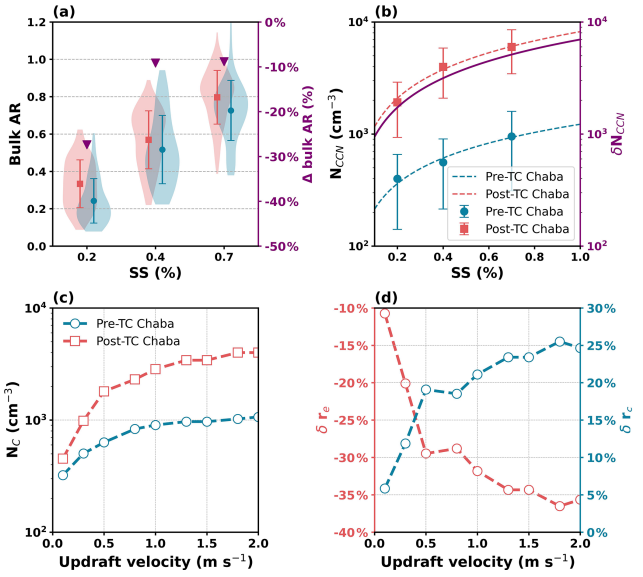


Figure 5. **(a)** The bulk activation ratio (AR) at different supersaturations (SS), the fitting result between the N_{CCN} and SS, and the change of N_{CCN} at different SS during pre-TC Chaba and post-TC Chaba periods; **(b)** The change of cloud effective radius (r_e) and critical radius (r_c) at different SS; **(c)** The simulated cloud droplet (N_C) at different updraft velocity in different periods; **(d)** The average liquid cloud particle size from Modis data during pre-TC Chaba and post-TC Chaba period; It is noted that r_e and r_c refer to the Twomey effect and Albrecht effect, respectively.

groscopicity changes associated with OA loading are not adequately captured. Incorporating composition-dependent hygroscopicity parameterizations may therefore be necessary to reduce biases in simulated N_{CCN} or N_C over such regions.

Our results highlight the potential for TCs to influence aerosol–cloud interactions by transporting anthropogenic aerosols from continental regions to the marine atmosphere. This transport can increase aerosol number concentrations and cloud condensation nuclei (CCN), leading to more activated cloud droplets and smaller r_e, with potential implications for cloud albedo and the radiative balance. MODIS observations showed decreases of approximately 2–3 µm in r_e over the western region of TC Chaba and two TCs that formed over the South China Sea (SCS) in 2021 and followed similar tracks (Figs. 6, S17–S18). The r_e were averaged over the same regions as those defined in Sect. 2.3.5. For TC Chaba, the decrease was approximately 11 %, consistent with our simulations at an updraft velocity of 0.1 m s^{-1}. This may be attributed to TC-induced circulation changes that facilitated the transport of terrestrial aerosols to the marine environment. The resulting elevation in NCCN subsequently increased NC, restricting individual droplet growth due to competition for available water vapor. Although these satellite-derived changes may also reflect variations in cloud type, updraft velocity, liquid water path, cloud-top height, precipitation, and TC dynamics, aerosol effects may have contributed. This interpretation is consistent with aircraft observations over the SCS showing higher concentrations of small droplets and fewer mid-sized droplets in clouds influenced by industrial and biomass-burning aerosols than in clean marine clouds (Miller et al., 2023).

However, TC-related precipitation can counteract circulation-driven increases in aerosol concentrations through wet scavenging. The inner and outer rainbands typically extend to approximately 200 and 500 km from the TC center, respectively, although their size and structure vary considerably among TCs (Addington et al., 2025). During our observations, the vessel approached within approximately 446 km of Chaba's center, but no prolonged period of substantial precipitation occurred. Although previous studies have reported extensive outer-rainband precipitation 200–500 km from TC centers, particularly under favorable moisture conditions (Hence and Houze, 2012; Addington et al., 2025), the limited precipitation during our campaign suggests that the observed aerosol changes primarily reflect TC-related transport and associated atmospheric processes rather than sustained wet removal. Nevertheless, precipitation may have affected aerosol properties during individual periods, as observed on 1 July.

These findings may have broader implications under climate change. Although the frequency of TCs affecting the SCS exhibits complex variability (Huang et al., 2022a), previous studies suggest that the intensity of both locally formed TCs and westward-moving TCs from the western North Pacific has increased (Mei and Xie, 2016; Kossin et al., 2016). If these trends continue, TCs may repeatedly transport anthropogenic aerosols into marine regions, altering aerosol properties and cloud microphysics, particularly in their outer regions. Regional climate and weather prediction models should therefore consider TC-driven aerosol transport and its interactions with cloud microphysics when assessing future changes in the SCS aerosol–cloud system.

Finally, it should be noted that this study is based on a single TC case and is constrained by the lack of direct in situ cloud microphysical measurements. Future work should expand to more TC events and incorporate direct observations of cloud microphysical parameters to better quantify the robustness and climatic relevance of the processes identified here. Given projected increases in TC intensity over the SCS (Liu and Chan, 2020) such efforts are essential for improving our understanding of regional aerosol–cloud interactions and their implications for climate forcing and precipitation variability.

5 Conclusions

Based on shipborne observations over the South China Sea (SCS), this study investigated the effects of Tropical Cyclone (TC) Chaba on marine aerosols and aerosol–cloud interactions in its western region. TC-related circulation trans-

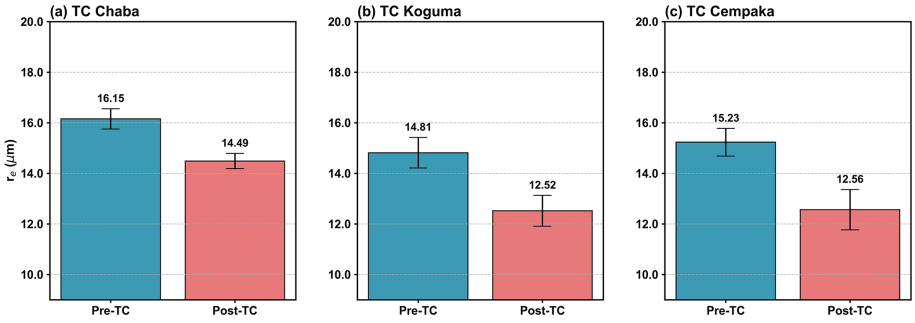


Figure 6. The cloud effective radius (r_e) from modis data during pre-TC Chaba Period and post-TC Chaba period **(a)**; The r_e during pre-TC Koguma Period and post-TC Koguma period **(b)**; The r_e during pre-TC Cempaka Period and post-TC Cempaka period **(c)**.

ported anthropogenic aerosols from the Indochina Peninsula, increasing non-refractory submicron particulate matter ($NR\text{-}PM_1$) concentrations from 4.51 to 8.84 $\mu g\,m^{-3}$. The organic aerosol (OA) fraction increased from 14.6 % to 44.9 %, mainly due to oxygenated organic aerosols (OOA). This compositional shift was accompanied by an approximately 60 % decrease in bulk aerosol hygroscopicity (κ), from 0.58–0.66 to 0.20–0.31 across supersaturations (SS) of 0.2 %–0.7 %.

Despite a modest increase in aerosol effective diameter of approximately 4 % (from 92 to 96 nm), the decrease in hygroscopicity reduced the bulk activation ratio (AR) from 0.33–0.80 to 0.24–0.73. However, the substantial increase in aerosol number concentrations led to up to sixfold higher CCN concentrations, from 400–951 to 1918–5981 cm^{-3}. Cloud parcel model simulations indicated that the enhanced CCN concentrations reduced cloud droplet effective radius (r_e) by 11 %–37 % and increased the critical radius for autoconversion by 6 %–26 %. The MODIS observations of TC Chaba and two TCs over the SCS in 2021 also showed decreases in r_e, providing independent observational evidence consistent with the simulations, although other meteorological factors may have contributed.

Overall, our findings show that TC-driven aerosol transport can substantially alter aerosol composition, hygroscopicity, CCN activation, and cloud microphysics over the SCS. These results highlight the need for regional climate and weather prediction models to account for composition-dependent aerosol hygroscopicity and TC-related aerosol transport when simulating CCN and aerosol–cloud interactions. Given projections of increasing TC intensity under climate change, the potential effects of TC-driven aerosol perturbations on regional cloud properties and precipitation need further investigation.

Data availability. The aerosol composition, meteorology, trace gas, cloud condensation nuclei, and aerosol hygroscopicity data from field measurements can be found on https://doi.org/10.6084/m9.figshare.32414736 (Ou, 2026); The weekly GDAS1 (Global Data Assimilation System, 1° resolution) meteorological fields can be obtained from the NOAA Air Resources Laboratory (ARL) (https://www.ready.noaa.gov/gdas1.php, last access: 12 December 2025); The MCD06COSP_D3_MODIS product can be found on https://doi.org/10.5067/MODIS/MCD06COSP_D3_MODIS.062 (NASA, 2026).

Supplement. The supplement related to this article is available online at https://doi.org/10.5194/acp-26-16667-2026-supplement.

Author contributions. M. C. and H. W. designed the study and drafted the original manuscript. H. O. conducted data collection on board, performed the data analysis, and drafted the original manuscript. X. N., S. M., Q. S., and B. L. conducted data collection on board. T. D., J. S., and S. Z. contributed to improving the original manuscript. J. Z. designed the field measurement.

Competing interests. The contact author has declared that none of the authors has any competing interests.

Disclaimer. Publisher's note: Copernicus Publications remains neutral with regard to jurisdictional claims made in the text, published maps, institutional affiliations, or any other geographical representation in this paper. The authors bear the ultimate responsibility for providing appropriate place names. Views expressed in the text are those of the authors and do not necessarily reflect the views of the publisher.

Acknowledgements. We thank Professor Jun Zhao for his support and guidance throughout this study. We also thank the crew members of R/V *Sun* Yat-sen University and our colleagues for their assistance during the shipborne measurement campaign.

Financial support. This work was supported by National Natural Science Foundation of China (grant no. 42305123, 42175115), Guangdong Basic and Applied Basic Research Foundation (grant no. 2024A1515030221), Science and Technology Projects in Guangzhou (grant no. 2025A04J4493), Guangdong S&T Program (2026B1111020001), the Key Innovation Team of Guangdong Meteorological Bureau (grant no. GRMCTD202506-ZD06), Central Public interest Scientific Institution Basal Research Fund of South China Institute of Environmental Sciences, MEE (grant no. PM-zx097-202506-214), and Basic Research Fund of the Institute of Tropical and Marine Meteorology of China Meteorological Administration (grant no. RDS202502).

Review statement. This paper was edited by Guangjie Zheng and reviewed by two anonymous referees.

References

Addington, K. D., Zick, S. E., Wood, K. M., Matyas, C. J., and Berislavich, K.: Variations in Tropical Cyclone Size and Rainfall Patterns Based on Synoptic-Scale Moisture Environments in the North Atlantic, J. Geophys. Res.-Atmos., 130, e2024JD043135, https://doi.org/10.1029/2024JD043135, 2025.

Albrecht, B. A.: Aerosols, cloud microphysics, and fractional cloudiness, Science, 245, 1227–1230, https://doi.org/10.1126/science.245.4923.1227, 1989.

Atwood, S. A., Reid, J. S., Kreidenweis, S. M., Blake, D. R., Jonsson, H. H., Lagrosas, N. D., Xian, P., Reid, E. A., Sessions, W. R., and Simpas, J. B.: Size-resolved aerosol and cloud condensation nuclei (CCN) properties in the remote marine South China Sea – Part 1: Observations and source classification, Atmos. Chem. Phys., 17, 1105–1123, https://doi.org/10.5194/acp-17-1105-2017, 2017.

Bhatti, Y. A., Watson-Parris, D., Regayre, L. A., Jia, H., Neubauer, D., Im, U., Svenhag, C., Schutgens, N., Tsikerdekis, A., Nenes, A., Irfan, M., van Diedenhoven, B., Arifi, A., Fu, G., and Hasekamp, O. P.: Uncertainty in aerosol effective radiative forcing from anthropogenic and natural aerosol parameters in ECHAM6.3-HAM2.3, Atmos. Chem. Phys., 26, 269–293, https://doi.org/10.5194/acp-26-269-2026, 2026.

Bhattu, D., Tripathi, S. N., and Chakraborty, A.: Deriving aerosol hygroscopic mixing state from size-resolved CCN activity and HR-ToF-AMS measurements, Atmos Environ., 142, 57–70, https://doi.org/10.1016/j.atmosenv.2016.07.032, 2016.

Black, M. L., Burpee, R. W., and Marks, F. D.: Vertical Motion Characteristics of Tropical Cyclones Determined with Airborne Doppler Radial Velocities, J. Atmos. Sci., 53, 1887–1909, https://doi.org/10.1175/1520-0469(1996)053<1887:VMCOTC>2.0.CO;2, 1996.

Boucher, O. and Lohmann, U.: The sulfate-CCN-cloud albedo effect, Tellus B, 47, 281–300, https://doi.org/10.3402/tellusb.v47i3.16048, 1995.

Cai, M., Tan, H., Chan, C. K., Qin, Y., Xu, H., Li, F., Schurman, M. I., Liu, L., and Zhao, J.: The size-resolved cloud condensation nuclei (CCN) activity and its prediction based on aerosol hygroscopicity and composition in the Pearl Delta River (PRD) region during wintertime 2014, Atmos. Chem. Phys., 18, 16419–16437, https://doi.org/10.5194/acp-18-16419-2018, 2018.

Cai, M., Liang, B., Sun, Q., Zhou, S., Chen, X., Yuan, B., Shao, M., Tan, H., and Zhao, J.: Effects of continental emissions on cloud condensation nuclei (CCN) activity in the northern South China Sea during summertime 2018, Atmos. Chem. Phys., 20, 9153–9167, https://doi.org/10.5194/acp-20-9153-2020, 2020.

Chen, J., Zhu, W., Liu, Q., Qian, X., Chen, X., Zheng, J., Yang, T., Xu, Q., and Yang, T.: Temporal Evolution and Regional Properties of Aerosol over the South China Sea, Remote Sens., 15, 501, https://doi.org/10.3390/rs15020501, 2023.

Chen, L., Li, Y., and Cheng, Z.: An overview of research and forecasting on rainfall associated with landfalling tropical cyclones, Adv. Atmos. Sci, 27, 967–976, https://doi.org/10.1007/s00376-010-8171-y, 2010.

Chen, Y.-C., Christensen, M. W., Stephens, G. L., and Seinfeld, J. H.: Satellite-based estimate of global aerosol–cloud radiative forcing by marine warm clouds, Nat. Geosci, 7, 643–646, https://doi.org/10.1038/ngeo2214, 2014.

Dusek, U., Frank, G. P., Hildebrandt, L., Curtius, J., Schneider, J., Walter, S., Chand, D., Drewnick, F., Hings, S., Jung, D., Borrmann, S., and Andreae, M. O.: Size Matters More Than Chemistry for Cloud-Nucleating Ability of Aerosol Particles, Science, 312, 1375–1378, https://doi.org/10.1126/science.1125261, 2006.

Geller, M., Biswas, S., and Sioutas, C.: Determination of Particle Effective Density in Urban Environments with a Differential Mobility Analyzer and Aerosol Particle Mass Analyzer, Aerosol Sci. Tech., 40, 709–723, https://doi.org/10.1080/02786820600803925, 2006.

Hence, D. A. and Houze, R. A.: Vertical Structure of Tropical Cyclone Rainbands as Seen by the TRMM Precipitation Radar, J. Atmos. Sci., 69, 2644–2661, https://doi.org/10.1175/JAS-D-11-0323.1, 2012.

Huang, P., Xu, J., and Liang, M.: Decadal variation in the frequency of tropical cyclones originating in the South China Sea and migrating from the western North Pacific, Front. Earth Sci, 10, https://doi.org/10.3389/feart.2022.980220, 2022a.

Huang, S., Wu, Z., Wang, Y., Poulain, L., Höpner, F., Merkel, M., Herrmann, H., and Wiedensohler, A.: Aerosol Hygroscopicity and its Link to Chemical Composition in a Remote Marine Environment Based on Three Transatlantic Measurements, Environ. Sci. Technol., 56, 9613–9622, https://doi.org/10.1021/acs.est.2c00785, 2022b.

IPCC: Annex I: Observational Products [Trewin, B. (ed.)], in: Climate Change 2021: The Physical Science Basis. Contribution of Working Group I to the Sixth Assessment Report of the Intergovernmental Panel on Climate Change, edited by: Masson-Delmotte, V., Zhai, P., Pirani, A., Connors, S. L., Péan, C., Berger, S., Caud, N., Chen, Y., Goldfarb, L., Gomis, M. I., Huang, M., Leitzell, K., Lonnoy, E., Matthews, J. B. R., Maycock, T. K., Waterfield, T., Yelekçi, O., Yu, R., and Zhou, B., Cambridge University Press, Cambridge, United Kingdom and New York, NY, USA, 2061–2086, https://doi.org/10.1017/9781009157896.015, 2021.

Jose, S., Nair, V. S., and Babu, S. S.: Anthropogenic emissions from South Asia reverses the aerosol indirect effect over the northern Indian Ocean, Sci. Rep., 10, 18360, https://doi.org/10.1038/s41598-020-74897-x, 2020.

Kawana, K., Miyazaki, Y., Omori, Y., Tanimoto, H., Kagami, S., Suzuki, K., Yamashita, Y., Nishioka, J., Deng, Y., Yai, H., and Mochida, M.: Number-Size Distribution and CCN Activity of Atmospheric Aerosols in the Western North Pacific During Spring Pre-Bloom Period: Influences of Terrestrial and Marine Sources, J. Geophys. Res.-Atmos., 127, e2022JD036690, https://doi.org/10.1029/2022jd036690, 2022.

King, S. M., Butcher, A. C., Rosenoern, T., Coz, E., Lieke, K. I., de Leeuw, G., Nilsson, E. D., and Bilde, M.: Investigating Primary Marine Aerosol Properties: CCN Activity of Sea Salt and Mixed Inorganic–Organic Particles, Environ. Sci. Technol., 46, 10405–10412, https://doi.org/10.1021/es300574u, 2012.

Kossin, J. P., Emanuel, K. A., and Camargo, S. J.: Past and Projected Changes in Western North Pacific Tropical Cyclone Exposure, J. Clim, 29, 5725–5739, https://doi.org/10.1175/JCLI-D-16-0076.1, 2016.

Kristensen, T. B., Müller, T., Kandler, K., Benker, N., Hartmann, M., Prospero, J. M., Wiedensohler, A., and Stratmann, F.: Properties of cloud condensation nuclei (CCN) in the trade wind marine boundary layer of the western North Atlantic, Atmos. Chem. Phys., 16, 2675–2688, https://doi.org/10.5194/acp-16-2675-2016, 2016.

Kuwata, M. and Kondo, Y.: Dependence of size-resolved CCN spectra on the mixing state of nonvolatile cores observed in Tokyo, J. Geophys. Res.-Atmos., 113, https://doi.org/10.1029/2007JD009761, 2008.

Lathem, T. L. and Nenes, A.: Water Vapor Depletion in the DMT Continuous-Flow CCN Chamber: Effects on Supersaturation and Droplet Growth, Aerosol Sci. Tech., 45, 604–615, https://doi.org/10.1080/02786826.2010.551146, 2011.

Liang, B., Cai, M., Sun, Q., Zhou, S., and Zhao, J.: Source apportionment of marine atmospheric aerosols in northern South China Sea during summertime 2018, Environ. Pollut., 289, 117948, https://doi.org/10.1016/j.envpol.2021.117948, 2021.

Lin, X. and Huang, G.: Assessing Tropical Cyclone-Driven Aerosol Transport – A High-Resolution WRF-Chem Analysis of Major Hurricane Matthew and Implications for Future Climate Scenarios, Environ. Sci. Technol., 59, 9060–9071, https://doi.org/10.1021/acs.est.5c02251, 2025.

Liu, K. S. and Chan, J. C. L.: Recent increase in extreme intensity of tropical cyclones making landfall in South China, Clim. Dynam., 55, 1059–1074, https://doi.org/10.1007/s00382-020-05311-5, 2020.

Liu, L.-Y., Wei, G.-L., Wang, J.-Z., Guan, Y.-F., Wong, C. S., Wu, F.-C., and Zeng, E. Y.: Anthropogenic Activities Have Contributed Moderately to Increased Inputs of Organic Materials in Marginal Seas off China, Environ. Sci. Technol., 47, 11414–11422, https://doi.org/10.1021/es401751k, 2013.

Liu, Y., Daum, P. H., McGraw, R., and Miller, M.: Generalized threshold function accounting for effect of relative dispersion on threshold behavior of autoconversion process, Geophys. Res. Lett., 33, https://doi.org/10.1029/2005GL025500, 2006.

Liu, Y., Daum, P. H., Guo, H., and Peng, Y.: Dispersion bias, dispersion effect, and the aerosol–cloud conundrum, Environ. Res. Lett, 3, 045021, https://doi.org/10.1088/1748-9326/3/4/045021, 2008.

Lu, M.-L. and Seinfeld, J. H.: Study of the Aerosol Indirect Effect by Large-Eddy Simulation of Marine Stratocumulus, J. Atmos. Sci., 62, 3909–3932, https://doi.org/10.1175/JAS3584.1, 2005.

Mallet, M. D., D'Anna, B., Même, A., Bove, M. C., Cassola, F., Pace, G., Desboeufs, K., Di Biagio, C., Doussin, J.-F., Maille, M., Massabò, D., Sciare, J., Zapf, P., di Sarra, A. G., and Formenti, P.: Summertime surface PM1 aerosol composition and size by source region at the Lampedusa island in the central Mediterranean Sea, Atmos. Chem. Phys., 19, 11123–11142, https://doi.org/10.5194/acp-19-11123-2019, 2019.

McFiggans, G., Artaxo, P., Baltensperger, U., Coe, H., Facchini, M. C., Feingold, G., Fuzzi, S., Gysel, M., Laaksonen, A., Lohmann, U., Mentel, T. F., Murphy, D. M., O'Dowd, C. D., Snider, J. R., and Weingartner, E.: The effect of physical and chemical aerosol properties on warm cloud droplet activation, Atmos. Chem. Phys., 6, 2593–2649, https://doi.org/10.5194/acp-6-2593-2006, 2006.

Mei, W. and Xie, S.-P.: Intensification of landfalling typhoons over the northwest Pacific since the late 1970s, Nat. Geosci., 9, 753–757, https://doi.org/10.1038/ngeo2792, 2016.

Meng, J. W., Yeung, M. C., Li, Y. J., Lee, B. Y. L., and Chan, C. K.: Size-resolved cloud condensation nuclei (CCN) activity and closure analysis at the HKUST Supersite in Hong Kong, Atmos. Chem. Phys., 14, 10267–10282, https://doi.org/10.5194/acp-14-10267-2014, 2014.

Miles, N. L., Verlinde, J., and Clothiaux, E. E.: Cloud Droplet Size Distributions in Low-Level Stratiform Clouds, J. Atmos. Sci., 57, 295–311, https://doi.org/10.1175/1520-0469(2000)057<0295:CDSDIL>2.0.CO;2, 2000.

Miller, R. M., Rauber, R. M., Di Girolamo, L., Rilloraza, M., Fu, D., McFarquhar, G. M., Nesbitt, S. W., Ziemba, L. D., Woods, S., and Thornhill, K. L.: Influence of natural and anthropogenic aerosols on cloud base droplet size distributions in clouds over the South China Sea and West Pacific, Atmos. Chem. Phys., 23, 8959–8977, https://doi.org/10.5194/acp-23-8959-2023, 2023.

Moore, R. H., Nenes, A., and Medina, J.: Scanning Mobility CCN Analysis – A Method for Fast Measurements of Size-Resolved CCN Distributions and Activation Kinetics, Aerosol Sci. Tech., 44, 861–871, https://10.1080/02786826.2010.498715, 2010.

NASA: MCD06COSP_D3_MODIS – MODIS (Aqua/Terra) Cloud Properties Level 3 daily, 1×1 degree grid, LAADS DAAC [data set], https://doi.org/10.5067/MODIS/MCD06COSP_D3_MODIS.062, 2026.

Ng, N. L., Canagaratna, M. R., Jimenez, J. L., Zhang, Q., Ulbrich, I. M., and Worsnop, D. R.: Real-Time Methods for Estimating Organic Component Mass Concentrations from Aerosol Mass Spectrometer Data, Environ. Sci. Technol., 45, 910–916, https://doi.org/10.1021/es102951k, 2011a.

Ng, N. L., Herndon, S. C., Trimborn, A., Canagaratna, M. R., Croteau, P. L., Onasch, T. B., Sueper, D., Worsnop, D. R., Zhang, Q., Sun, Y. L., and Jayne, J. T.: An Aerosol Chemical Speciation Monitor (ACSM) for Routine Monitoring of the Composition and Mass Concentrations of Ambient Aerosol, Aerosol Sci. Tech., 45, 780–794, https://doi.org/10.1080/02786826.2011.560211, 2011b.

Ou, H.: Aerosol, meteorology, trace gas and cloud condensation nuclei data for field measurement on Sun Yat-sen Vessel in South China Sea in 2022, figshare [data set], https://doi.org/10.6084/m9.figshare.32414736.v1, 2026.

Ou, H., Cai, M., Zhang, Y., Ni, X., Liang, B., Sun, Q., Mai, S., Sun, C., Zhou, S., Wang, H., Sun, J., and Zhao, J.: Mea-

surement report: Cloud condensation nuclei (CCN) activity in the South China Sea from shipborne observations during the summer and winter of 2021 – seasonal variation and anthropogenic influence, Atmos. Chem. Phys., 25, 2495–2513, https://doi.org/10.5194/acp-25-2495-2025, 2025.

Ovadnevaite, J., Čeburnis, D., Kvietkus, K., Rimšelyte, I., and Pesliakait, E.: Chemical Composition and Size Distribution of Fine Aerosol Particles Measured with AMS on the East Coast of the Baltic Sea, Nucleation and Atmospheric Aerosols, Dordrecht, 792–796, https://doi.org/10.1007/978-1-4020-6475-3_157, 20077

Pérez-Alarcón, A., Sorí, R., Fernández-Alvarez, J. C., Nieto, R., and Gimeno, L.: Comparative climatology of outer tropical cyclone size using radial wind profiles, Weather Clim. Extrem., 33, 100366, https://doi.org/10.1016/j.wace.2021.100366, 2021.

Petters, M. D. and Kreidenweis, S. M.: A single parameter representation of hygroscopic growth and cloud condensation nucleus activity, Atmos. Chem. Phys., 7, 1961–1971, https://doi.org/10.5194/acp-7-1961-2007, 2007.

Platnick, S., Meyer, K. G., King, M. D., Wind, G., Amarasinghe, N., Marchant, B., Arnold, G. T., Zhang, Z., Hubanks, P. A., Holz, R. E., Yang, P., Ridgway, W. L., and Riedi, J.: The MODIS Cloud Optical and Microphysical Products: Collection 6 Updates and Examples From Terra and Aqua, IEEE T. Geosci. Remote Sens., 55, 502–525, https://doi.org/10.1109/TGRS.2016.2610522, 2017.

Pöhlker, M. L., Pöhlker, C., Ditas, F., Klimach, T., Hrabe de Angelis, I., Araújo, A., Brito, J., Carbone, S., Cheng, Y., Chi, X., Ditz, R., Gunthe, S. S., Kesselmeier, J., Könemann, T., Lavrič, J. V., Martin, S. T., Mikhailov, E., Moran-Zuloaga, D., Rose, D., Saturno, J., Su, H., Thalman, R., Walter, D., Wang, J., Wolff, S., Barbosa, H. M. J., Artaxo, P., Andreae, M. O., and Pöschl, U.: Long-term observations of cloud condensation nuclei in the Amazon rain forest – Part 1: Aerosol size distribution, hygroscopicity, and new model parametrizations for CCN prediction, Atmos. Chem. Phys., 16, 15709–15740, https://doi.org/10.5194/acp-16-15709-2016, 2016.

Qin, Y., Wang, H., Wang, Y., Lu, X., Tang, H., Zhang, J., Li, L., and Fan, S.: Wildfires in Southeast Asia pollute the atmosphere in the northern South China Sea, Sci. Bull., 69, 1011–1015, https://doi.org/10.1016/j.scib.2024.02.026, 2024.

Qiu, S., Zheng, X., Painemal, D., Terai, C. R., and Zhou, X.: Daytime variation in the aerosol indirect effect for warm marine boundary layer clouds in the eastern North Atlantic, Atmos. Chem. Phys., 24, 2913–2935, https://doi.org/10.5194/acp-24-2913-2024, 2024.

Quaas, J., Boucher, O., and Bréon, F. M.: Aerosol indirect effects in POLDER satellite data and the Laboratoire de Météorologie Dynamique–Zoom (LMDZ) general circulation model, J. Geophys. Res.-Atmos., 109, https://doi.org/10.1029/2003JD004317, 2004.

Regayre, L. A., Schmale, J., Johnson, J. S., Tatzelt, C., Baccarini, A., Henning, S., Yoshioka, M., Stratmann, F., Gysel-Beer, M., Grosvenor, D. P., and Carslaw, K. S.: The value of remote marine aerosol measurements for constraining radiative forcing uncertainty, Atmos. Chem. Phys., 20, 10063–10072, https://doi.org/10.5194/acp-20-10063-2020, 2020.

Reutter, P., Su, H., Trentmann, J., Simmel, M., Rose, D., Gunthe, S. S., Wernli, H., Andreae, M. O., and Pöschl, U.: Aerosol- and updraft-limited regimes of cloud droplet formation: influence of particle number, size and hygroscopicity on the activation of cloud condensation nuclei (CCN), Atmos. Chem. Phys., 9, 7067–7080, https://doi.org/10.5194/acp-9-7067-2009, 2009.

Rotstayn, L. D. and Liu, Y.: Cloud droplet spectral dispersion and the indirect aerosol effect: Comparison of two treatments in a GCM, Geophys. Res. Lett., 36, https://doi.org/10.1029/2009GL038216, 2009.

Seifert, A. and Beheng, K. D.: A two-moment cloud microphysics parameterization for mixed-phase clouds. Part 1: Model description, Meteorol. Atmos. Phys, 92, 45–66, https://doi.org/10.1007/s00703-005-0112-4, 2006.

Shao, M., Yang, J., Wang, J., Chen, P., Liu, B., and Dai, Q.: Co-Occurrence of Surface O3, PM2.5 Pollution, and Tropical Cyclones in China, J. Geophys. Res.-Atmos., 127, e2021JD036310, https://doi.org/10.1029/2021JD036310, 2022.

Sun, Q., Liang, B., Cai, M., Zhang, Y., Ou, H., Ni, X., Sun, X., Han, B., Deng, X., Zhou, S., and Zhao, J.: Cruise observation of the marine atmosphere and ship emissions in South China Sea: Aerosol composition, sources, and the aging process, Environ. Pollut., 316, 120539, https://doi.org/10.1016/j.envpol.2022.120539, 2023.

Takami, A., Miyoshi, T., Shimono, A., and Hatakeyama, S.: Chemical composition of fine aerosol measured by AMS at Fukue Island, Japan during APEX period, Atmos. Environ., 39, 4913-4924, https://doi.org/10.1016/j.atmosenv.2005.04.038, 2005.

Twomey, S.: The nuclei of natural cloud formation part II: The supersaturation in natural clouds and the variation of cloud droplet concentration, Pure Appl. Geophys., 43, 243–249, https://doi.org/10.1007/BF01993560, 1959.

van den Born, M., Ou, H., Mulder, J., Fu, J., Saathoff, H., and Dusek, U.: Measurements of NaCl in ambient air with a capture vaporizer-ToF-ACSM, Aerosol Research, 4, 577–587, https://doi.org/10.5194/ar-4-577-2026, 2026.

Wall, C. J., Storelvmo, T., and Possner, A.: Global observations of aerosol indirect effects from marine liquid clouds, Atmos. Chem. Phys., 23, 13125–13141, https://doi.org/10.5194/acp-23-13125-2023, 2023.

Wang, G., Su, J., Ding, Y., and Chen, D.: Tropical cyclone genesis over the south China sea, J. Mar. Syst., 68, 318–326, https://doi.org/10.1016/j.jmarsys.2006.12.002, 2007.

Wang, H., Rasch, P. J., and Feingold, G.: Manipulating marine stratocumulus cloud amount and albedo: a process-modelling study of aerosol-cloud-precipitation interactions in response to injection of cloud condensation nuclei, Atmos. Chem. Phys., 11, 4237–4249, https://doi.org/10.5194/acp-11-4237-2011, 2011.

Wang, N., Huang, X., Xu, J., Wang, T., Tan, Z.-M., and Ding, A.: Typhoon-boosted biogenic emission aggravates cross-regional ozone pollution in China, Sci. Adv, 8, eabl6166, https://doi.org/10.1126/sciadv.abl6166, 2022.

Wang, S., Murakami, H., and Cooke, W. F.: Anthropogenic forcing changes coastal tropical cyclone frequency, npj Clim. Atmos. Sci., 6, 187, https://doi.org/10.1038/s41612-023-00516-x, 2023.

Wang, X., Wang, C., Han, G., Li, W., and Wu, X.: Effects of tropical cyclones on large-scale circulation and ocean heat transport in the South China Sea, Clim. Dynam., 43, 3351–3366, https://doi.org/10.1007/s00382-014-2109-5, 2014a.

Wang, Y., Lee, K.-H., Lin, Y., Levy, M., and Zhang, R.: Distinct effects of anthropogenic aerosols on tropical cyclones, Nat. Clim.

Change, 4, 368–373, https://doi.org/10.1038/nclimate2144, 2014b.

Wang, Y., Niu, S., Lv, J., Lu, C., Xu, X., Wang, Y., Ding, J., Zhang, H., Wang, T., and Kang, B.: A New Method for Distinguishing Unactivated Particles in Cloud Condensation Nuclei Measurements: Implications for Aerosol Indirect Effect Evaluation, Geophys. Res. Lett., 46, 14185–14194, https://doi.org/10.1029/2019gl085379, 2019.

Wang, Y. Q.: MeteoInfo: GIS software for meteorological data visualization and analysis, Meteorol. Appl., 21, 360–368, https://doi.org/10.1002/met.1345, 2014.

Webb, M. J., Andrews, T., Bodas-Salcedo, A., Bony, S., Bretherton, C. S., Chadwick, R., Chepfer, H., Douville, H., Good, P., Kay, J. E., Klein, S. A., Marchand, R., Medeiros, B., Siebesma, A. P., Skinner, C. B., Stevens, B., Tselioudis, G., Tsushima, Y., and Watanabe, M.: The Cloud Feedback Model Intercomparison Project (CFMIP) contribution to CMIP6, Geosci. Model Dev., 10, 359–384, https://doi.org/10.5194/gmd-10-359-2017, 2017.